Self-Sensing Actuation for Nanopositioning and Active-Mode Damping in Dual-Stage HDDs

Chee Khiang Pang, *Student Member, IEEE*, Guoxiao Guo, *Senior Member, IEEE*, Ben M. Chen, *Senior Member, IEEE*, and Tong Heng Lee, *Member, IEEE*

***Abstract*—Position sensors other than the R/W heads are not embedded into current hard-disk drives (HDDs) due to cost, resolution, and signal-to-noise ratio (SNR) issues. Moreover, the "optimal" location for placing these sensors is still unknown. In this paper, the Pb-Zr-Ti (PZT) elements in the PZT suspension-based microactuator are used as a secondary actuator and a displacement sensor simultaneously with self-sensing actuation. The proposed displacement estimation circuit produces an estimated PZT microactuator's displacement with high SNR and nanometer resolution comparable to that measured from the laser doppler vibrometer (LDV). A robust active mode damping controller is then designed to damp the PZT microactuator suspension's torsion modes and sway mode, as well as decoupling the HDD dual-stage servo into two distinct loops for individual sensitivity optimization. Our results show attenuation of PZT microactuator's suspension modes by 5 dB and sway mode by 30 dB with low sensitivity. A reduction of up to 20% in 3σ position error signal is also observed.**

***Index Terms*—Active-mode damping (AMD), dual-stage servo systems, self-sensing actuation (SSA).**

I. Introduction

In today's information explosion era, hard-disk drives (HDDs) find their applications in many home and portable electronic devices. As such, industries are striving for HDDs with smaller form factors and higher recording density simultaneously to meet the storage demands of consumers. These pushing factors translate into stringent requirements for servo positioning to enable high recording densities. With the demonstration of more than 200 kTPI (tracks per inch) at the end of 2002, the track density of HDD product is expected to double by the end of 2004.

Such a high-track density requires a higher precision servo system, which cannot be achieved by the current HDDs employing the voice coil motor (VCM) as the sole actuator. The VCM limits the bandwidth extension in the single-stage servo system because of its mechanical resonances and high frequency uncertainties. As such, dual-stage actuation is seen by many as the solution for next generation of HDDs. In a typical proposed dual-stage HDD, a small secondary actuator (e.g., PZT suspension-based microactuator or PZT microactuator for short) is appended piggyback on the VCM for fine positioning. As the effective stroke range of the PZT microactuator is limited, it is easily saturated, which leads to instability of the dual-stage servo system if unconsidered [4]. Also, the electrical and mechanical characteristics of the PZT element are still not well developed and understood. The stiffness of the suspension remains an issue, hence unlike optical drives where dual-stage actuation is introduced with much celebrated success, secondary actuation is still not implemented into current magnetic HDDs. Position error signal (PES) remains as the only available information for feedback control when there are now two distinct actuators to be controlled.

On adding sensors for active control in HDDs, Huang *et al.* [5] used rotational accelerometers to damp the VCM butterfly mode in a single stage HDD, Li *et al.* [8] split the two PZT strips in a PZT-actuated suspension and use one strip of PZT element as actuator and the other as sensor for active vibration control in a dual-stage HDD. While Lee *et al.* [7] used the PZT elements in the entire compound actuator solely as a position sensor.

In this paper, self-sensing actuation (SSA) employing the PZT element as a secondary actuator, and displacement sensor is explored simultaneously. This idea was first brought to the HDD industry by Sasaki in 1999, but since then no results were documented till recently where [17] and [11] appeared simultaneously. Yanado *et al.* [17] uses the strain and strain rate information from SSA for active vibration control of the PZT microactuator, using positive position feedback (PPF) and strain rate feedback (SRF), respectively. Pang *et al.* [11] focus on the SNR issues in using the PZT microactuator with SSA and use the PZT microactuator's displacement information for active-mode damping (AMD) of the PZT microactuator for dual-stage sensitivity optimization.

With the natural collocation of the actuator and sensor, we propose a simple and robust AMD controller for the PZT microactuator. Together with PES, the PZT microactuator's displacement information is used to decouple the dual-stage servo system into two loops for track-following controller design and individual sensitivity optimization. Our experimental and simulation results show the effectiveness of the proposed scheme.

This paper is organized as follows. Section II gives a brief introduction on dual-stage servo systems in HDD. Section II discusses about SSA and implements a collocated sensor circuit on the PZT microactuator. The dual-stage controller design

Manuscript received August 17, 2004; revised November 17, 2005. Recommended by Technical Editor M. Tomizuka.

C. K. Pang is with A*STAR Data Storage Institute, Singapore 117608, and also with the Department of Electrical and Computer Engineering, National University of Singapore, Singapore 117576, (e-mail: PANG_Chee_Khiang@dsi.a-star.edu.sg).

G. Guo is with A*STAR Data Storage Institute, Singapore 117608. (e-mail: Guo_Guoxiao@dsi.a-star.edu.sg).

B. M. Chen and T. H. Lee are with the Department of Electrical and Computer Engineering, National University of Singapore, Singapore 117576.(e-mail: bmchen@nus.edu.sg; eleleeth@nus.edu.sg).

Digital Object Identifier 10.1109/TMECH.2006.875560

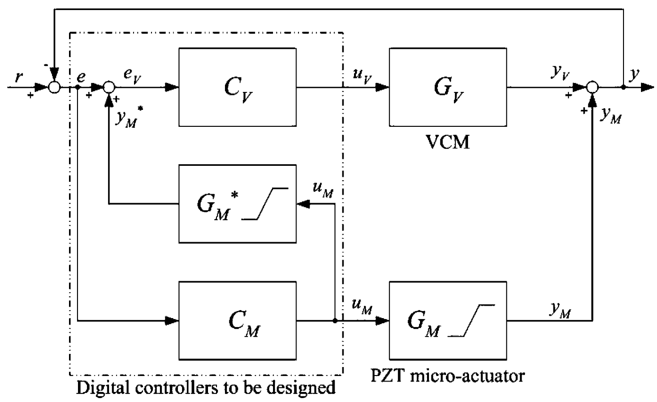

Fig. 1. Modified DMS configuration with PZT microactuator saturation considerations [4].

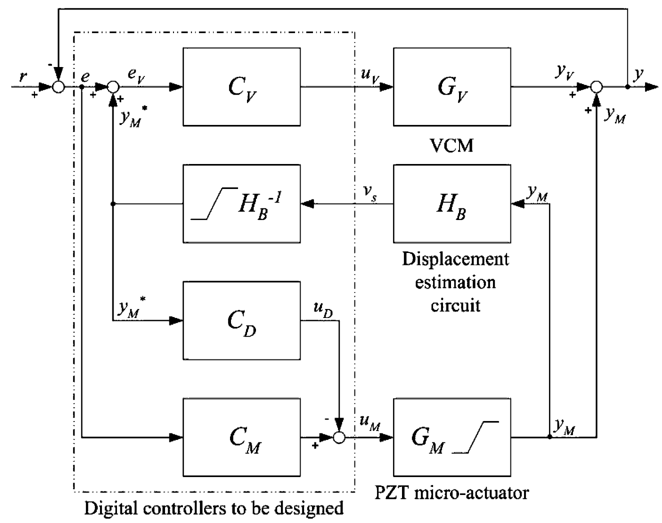

Fig. 2. Proposed SSA–DMS dual-stage control topology. The PZT microactuator's displacement estimation circuit H_{B} allows an online estimation of PZT microactuator's displacement y^*_{M}.

using the estimated PZT microactuator displacement for AMD and track following is proposed in Section IV. The performance of the proposed control scheme and experimental results are discussed in Section V. The conclusion and future work directions are summarized in Section VI.

II. Dual-Stage Servo Systems

The main classifications of HDD dual-stage servo systems in ascending order of size are: 1) the head based, where the microactuator is attached between the slider and the read/write head; 2) the slider based, where the microactuator is inserted between the suspension and the slider; and 3) the suspension based, where the microactuator is placed between the arm of the VCM and the suspension. Depending on the location in which the microactuator is placed, the control topology and design for a dual-stage HDD differs. The slider- and head-based microactuators are manufactured by the microelectromechanical system (MEMS) technology, and are hence known as MEMS microactuators. In our discussions and experiments, we are using the suspension-based microactuators actuated by PZT elements, or PZT microactuator for short.

Among the many dual-stage control designs proposed, the parallel configuration and the decoupled master–slave (DMS) configuration are the most widely used configurations. Readers referred to [14] for details on other control topologies. In the rest of the paper, we use the modified DMS dual-stage control structure with saturation as shown in Fig. 1 with $G_{\mathrm{V}}, G_{\mathrm{M}}, C_{\mathrm{V}}$, and C_{M} being the VCM, PZT microactuator, VCM controller, and PZT microactuator controller, respectively. This configuration is used for its simplicity and effectiveness in dealing with microactuator saturation issues [4].

In the DMS configuration, more control emphasis is placed on the microactuator (master) than the VCM (slave). This configuration constructs an off-line estimator G^*_{M} to predict the displacement of the secondary actuator y_{M}. As such, the VCM is driven by its decoupled loop error signal e_{V} as can be seen from Fig. 1. If G^*_{M} produces a good estimation y^*_{M} such that $y^*_{\mathrm{M}} \approx y_{\mathrm{M}}$, we can obtain decoupling of the two actuator loops. This enables individual loop control and sensitivity optimization for better disturbance rejection capabilities.

Because of the limited displacement range of the microactuator, the control efforts for the two actuators should be distributed properly when designing respective controllers to prevent saturation of the microactuator. An effective dual-stage loop should adhere to the guidelines given in [6] so that the actuators will not conflict with each other's control authority, causing negative interferences.

In this paper, we propose an SSA–DMS dual-stage control topology as shown in Fig. 2. Unlike the conventional DMS structure where only PES is used, this proposed SSA–DMS control topology uses PES and the estimated PZT microactuator's displacement y^*_{M} obtained from SSA for feedback control. The digital inverse of displacement estimation circuit $H_{\mathrm{B}}^{-1}(z)$ replaces the off-line estimator G^*_{M} in the conventional DMS configuration to obtain a real time estimated y^*_{M} for actively decoupling the dual-stage loop so that the controller designs and sensitivity optimization for the VCM and the PZT microactuator can be carried out independently. Further, y^*_{M} is also in AMD controller C_{D} to damp the PZT microactuator suspension's torsion modes and sway mode in the inner loop compensation, which was previously impossible if y^*_{M} arising from the displacement estimation circuit H_{B} using SSA was unavailable. The details on design of $C_{\mathrm{V}}, H_{\mathrm{B}}^{-1}, C_{\mathrm{D}}$, and C_{M} are presented in future sections.

III. Online Estimation of PZT Microactuator's Displacement Y^*_{m}

In this section, we shall detail the procedure in obtaining an online estimation of PZT microactuator's displacement y^*_{M}. The SNR and resolution of the estimated y^*_{M} will also be compared to the measured y_{M} from the LDV.

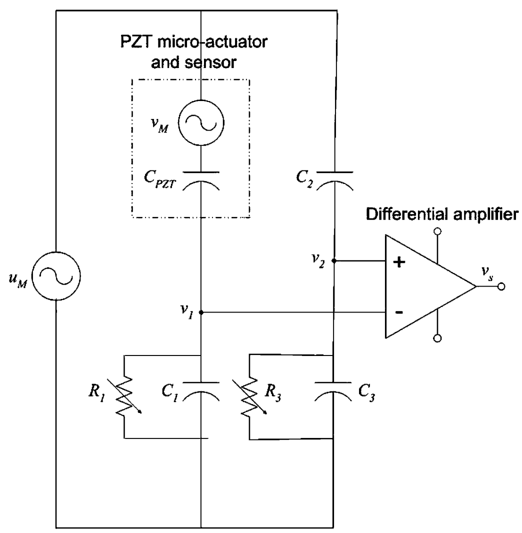

Fig. 3. Bridge circuit employing the PZT microactuator as actuator and sensor simultaneously. The PZT elements are modeled as a capacitor C_{PZT} with dependent voltage source v_{M}.

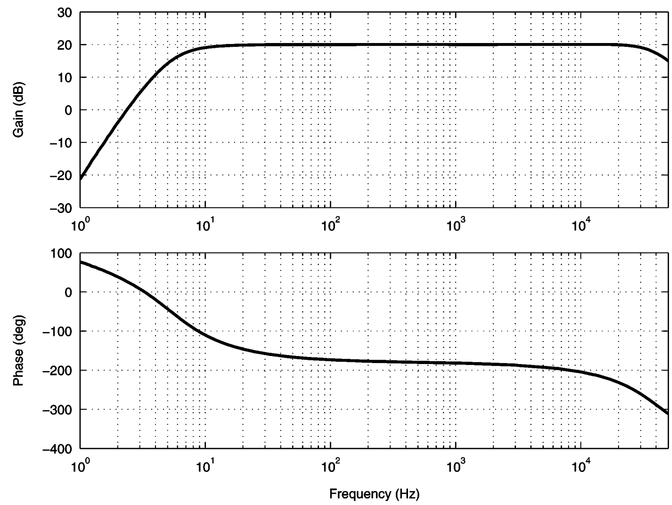

Fig. 4. Frequency response of differential amplifier setup consisting of HP1142A differential probe control and Brüel and Kjær voltage amplifier.

A. Self-Sensing Actuation (SSA)

When piezoelectric materials (e.g., PZT elements) are subjected to strain, charges arise on the surface of the material and hence setting up an electric field analogous to back electromotive force (EMF) in electromagnetic systems. This property allows the piezoelectric material to be used as an actuator and sensor simultaneously or common known as SSA. SSA has already been applied to many practical engineering problems (e.g., control of robot manipulators and cantilever beams; see [10] and the references therein). SSA is attractive in active control applications because the actuator and sensor arrangement is a truly collocated (or in many applications near collocated) pair, and hence avoids nonminimum phase zero dynamics, which degrades tracking performance.

In a PZT microactuator, the PZT elements can be modeled as a capacitance in series with a variable voltage source, the capacitor representing the dipoles, and the variable voltage source representing the electric field setup by the dipoles during actuation. If the capacitance of the PZT elements is known, we can decouple the variable voltage (hence strain/displacement information) using a bridge circuit. For our application, we construct a bridge circuit shown in [10] to generate displacement (proportional to strain) required for active control.

B. Bridge Circuit

The PZT elements in the PZT microactuator are modelled as a capacitor C_{PZT} in series with a dependent voltage source v_{M}, as shown in Fig. 3.

When the bridge circuit is subjected to control voltage u_{M}, the PZT microactuator is actuated to give displacement y_{M}. The voltage v_{M} generated is hence proportional to y_{M} (arising from mechanical strain) of the PZT microactuator, and can then be decoupled from u_{M} using a differential amplifier. As such, we can obtain the following equations from Fig. 3:

$$v_1 = \frac{C_{\mathrm{PZT}}}{C_1 + C_{\mathrm{PZT}}}(u_{\mathrm{M}} - v_{\mathrm{M}}) \tag{1}$$

$$v_2 = \frac{C_2}{C_2 + C_3}u_{\mathrm{M}} \tag{2}$$

$$\begin{aligned} v_{\mathrm{s}} &= v_2 - v_1 \\ &= \left(\frac{C_{\mathrm{PZT}}}{C_1 + C_{\mathrm{PZT}}} - \frac{C_2}{C_2 + C_3}\right)u_{\mathrm{M}} \\ &\quad + \frac{C_{\mathrm{PZT}}}{C_1 + C_{\mathrm{PZT}}}v_{\mathrm{M}}. \end{aligned} \tag{3}$$

The measured capacitance C_{PZT} of the PZT elements in the PZT microactuator is 160 μF. Resistors R_1 and R_3 are sometimes placed in parallel with capacitors C_1 and C_3 to prevent dc drifts. By making capacitors $C_1 = C_2 = C_3 = C_{\mathrm{PZT}}$, the bridge circuit is balanced and a PZT microactuator displacement estimator is established with

$$\begin{aligned} v_{\mathrm{s}} &= \frac{C_{\mathrm{PZT}}}{C_1 + C_{\mathrm{PZT}}}v_{\mathrm{M}} \\ &= \frac{v_{\mathrm{M}}}{2}. \end{aligned} \tag{4}$$

As such, v_{M} is decoupled from the control signal u_{M} and can be used for control purposes. Moreover, when applied to dual-stage HDDs, SSA requires only additional cheap electronic circuitry and does not reduce the effective actuation of the PZT microactuator. The only tradeoff we have is that a larger control signal u_{M} is needed for the same amount of displacement actuation as compared to no-bridge circuit.

For our experiments, a differential amplifier setup consisting of the HP1142A differential probe control (with power module) and Brüel and Kjær voltage amplifier for low noise and high gain amplification is used. The frequency response of the differential amplifier setup with a gain of 10 is shown in Fig. 4.

It should be noted that any high-speed low-noise instrumentation amplifiers (e.g., AD524 from Analog Devices) can be

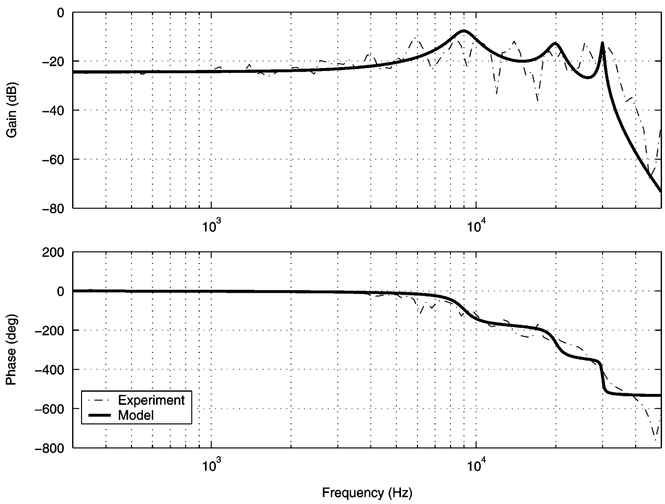

Fig. 5. Frequency response of displacement estimation circuit H_{B}.

TABLE I
PARAMETERS OF $H_{\mathrm{B}}(s)$

K_B	0.06
ζ_1	0.2
ζ_2	0.09
ζ_3	0.03
ω_1	$2\pi 9 \times 10^3$
ω_2	$2\pi 20 \times 10^3$
ω_3	$2\pi 30 \times 10^3$
τ	$2\pi \times 10^3$

used. The differential amplifier setup has constant gain with little phase distortion from 100 Hz to 10 kHz.

C. Identification of Displacement Estimation Circuit H_{B}

The PZT microactuator displacement estimation circuit H_{B} consists of the PZT microactuator/sensor and the differential amplifier setup. As v_{M} (hence v_{s}) arises from $y_{\mathrm{M}}, H_{\mathrm{B}}$ should be modelled by a transfer function $H_{\mathrm{B}}(s) = (v_{\mathrm{s}}(s)/y_{\mathrm{M}}(s))$. Making the VCM stationary, we connect y_{M} measured from the laser doppler vibrometer (LDV) to channel 1 and v_{s} from the differential amplifier setup output to channel 2 of the dynamic signal analyzer HP 35670A (DSA). The frequency response of $H_{\mathrm{B}}(s)$ is measured with swept sine excitation and is shown in Fig. 5.

To identify $H_{\mathrm{B}}(s)$, the following sixth-order transfer function is used:

$$H_{\mathrm{B}}(s) = K_{\mathrm{B}} \frac{\omega_1^2}{s^2 + 2\zeta_1\omega_1 s + \omega_1^2} \frac{\omega_2^2}{s^2 + 2\zeta_2\omega_2 s + \omega_2^2} \times \frac{\omega_3^2}{\tau} \frac{s+\tau}{s^2 + 2\zeta_3\omega_3 s + \omega_3^2}. \tag{5}$$

The values of $K_{\mathrm{B}}, \zeta_{\mathrm{i}}, \omega_{\mathrm{i}}$, and τ for $i = 1, 2$, and 3 are shown in Table I.

D. Performance Analysis

A digital inverse of $H_{\mathrm{B}}(s)$, $H_{\mathrm{B}}^{-1}(z)$, is constructed at a sampling frequency f_{s} of 100 kHz to provide an estimate of the PZT microactuator displacement y_{M}^*. The model inverse $H_{\mathrm{B}}^{-1}(s)$ is constructed as

$$H_{\mathrm{B}}^{-1}(s) = \frac{\tau\omega_\beta^5}{K_{\mathrm{B}}\omega_1^2\omega_2^2\omega_3^2} \frac{s^2 + 2\zeta_1\omega_1 s + \omega_1^2}{(s+\tau)(s+\omega_\beta)} \times \frac{s^2 + 2\zeta_2\omega_2 s + \omega_2^2}{(s+\omega_\beta)^2} \frac{s^2 + 2\zeta_3\omega_3 s + \omega_3^2}{(s+\omega_\beta)^2} \tag{6}$$

where $\omega_\beta = (\pi f_{\mathrm{s}}/\beta)$ and $1 \le \beta < 1.2$ is usually chosen so that the $H_{\mathrm{B}}^{-1}(s)$ is realizable. The poles are chosen near the Nyquist frequency $f_{\mathrm{s}}/2$ to maximize the dynamic range of H_{B}^{-1}. A saturation function is also included to mimic the saturation of the PZT microactuator.

While a sixth-order transfer function is computationally intensive, it is still more efficient than the eight-order estimator G_{M}^* (digital PZT microactuator model as shown in Fig. 11) used in conventional DMS control structures. With the inverse dynamics available, v_{s} is channeled into the digital inverse $H_{\mathrm{B}}^{-1}(z)$ so that its output y_{M}^* estimates the PZT microactuator's displacement y_{M} measured using the LDV. This allows us to evaluate the effectiveness of PZT microactuator displacement estimation circuit H_{B} in nanoposition sensing for usage in the dual-stage HDDs.

1) SNR Analysis: For brevity but without loss of generality, the performance of the sensor circuit is examined with sinusoids of frequencies at 10 and 30 kHz for illustration purposes. This is done by making the VCM stationary and exciting the PZT microactuator with $u_{\mathrm{M}} = 10\,\sin(2\pi 10 \times 10^3 t)$ V and $u_{\mathrm{M}} = 10\,\sin(2\pi 30 \times 10^3 t)$ V, respectively. The time responses of the measured PZT microactuator's displacement y_{M} using a LDV and the estimated displacement y_{M}^* from the digital inverse $H_{\mathrm{B}}^{-1}(z)$ are shown in Figs. 6 and 7. The small phase

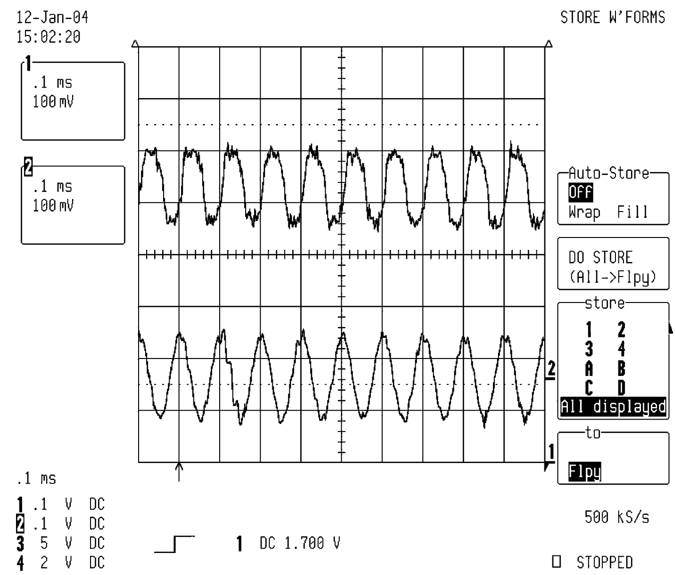

Fig. 6. Time responses with $u_{\mathrm{M}} = 10\,\sin(2\pi 10 \times 10^3 t)$ V. (Top) PZT microactuator's displacement y_{M} measured from LDV with resolution of 0.5 μm/V. (Bottom) Estimated PZT microactuator's displacement y_{M}^* from digital bridge circuit inverse $H_{\mathrm{B}}^{-1}(z)$. The PZT microactuator is actuating at about ± 37.5 nm in radial directions.

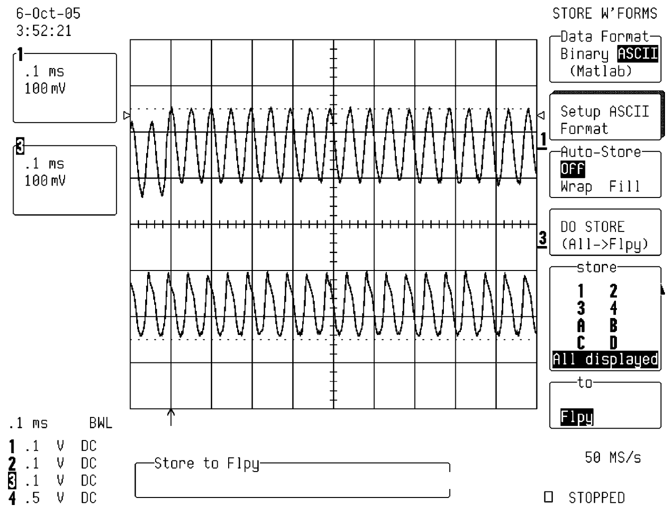

Fig. 7. Time responses with $u_{\mathrm{M}} = 10\ \sin(2\pi 30 \times 10^3 t)$ V. (Top) PZT microactuator's displacement y_{M} measured from LDV with resolution of 0.5μm/V. (Bottom) Estimated PZT microactuator's displacement y_{M}^* from digital bridge circuit inverse $H_{\mathrm{B}}^{-1}(z)$. The PZT microactuator is actuating at about ± 37.5 nm in radial directions.

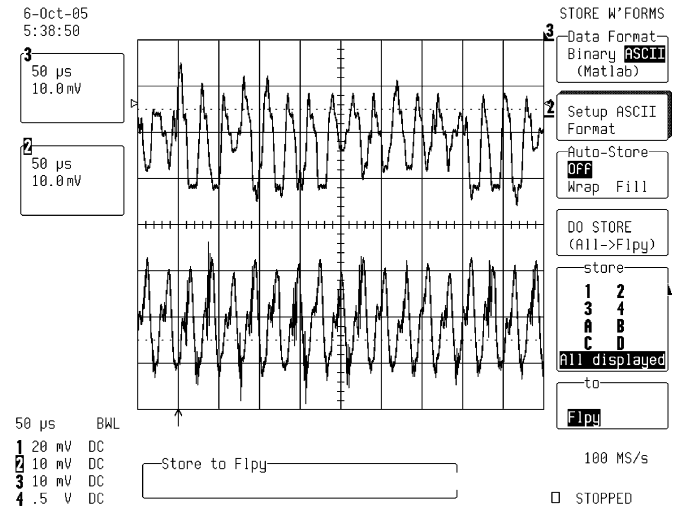

Fig. 9. Time responses with $u_{\mathrm{M}} = 1.2\ \sin(2\pi 30 \times 10^3 t)$ V. (Top) PZT microactuator's displacement y_{M} measured from LDV with resolution of 0.5μm/V. (Bottom) Estimated PZT microactuator's displacement y_{M}^* from digital bridge circuit inverse $H_{\mathrm{B}}^{-1}(z)$. The PZT microactuator is actuating at about ± 5 nm in radial directions.

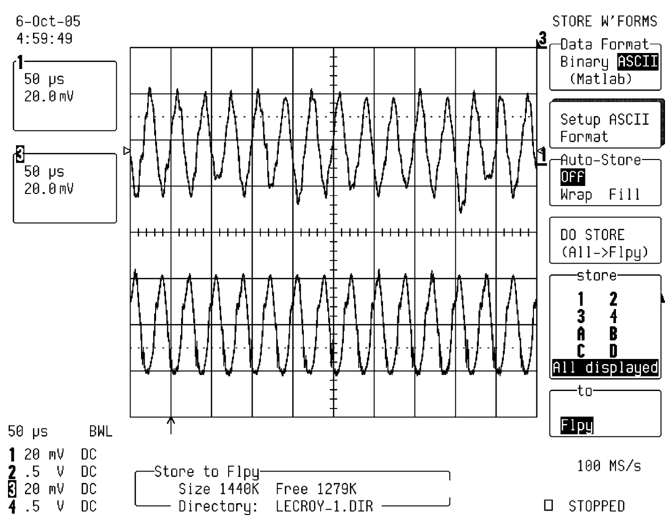

Fig. 8. Time responses with $u_{\mathrm{M}} = 2.5\ \sin(2\pi 30 \times 10^3 t)$ V. (Top) PZT microactuator's displacement y_{M} measured from LDV with resolution of 0.5μm/V. (Bottom) Estimated PZT microactuator's displacement y_{M}^* from digital bridge circuit inverse $H_{\mathrm{B}}^{-1}(z)$. The PZT microactuator is actuating at about ± 10 nm in radial directions.

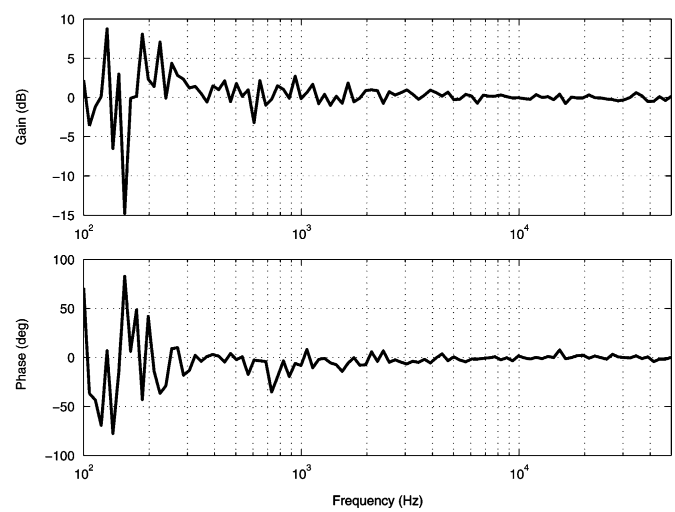

Fig. 10. Frequency response of measured PZT microactuator's displacement from LDV y_{M} to estimated PZT microactuator's displacement y_{M}^*. The PZT microactuator is set to actuate at about ± 8 nm in radial directions.

differences between the two signals are due to the phase loss during sampling and imperfect modeling of H_{B}.

If we reduce the source level of control signal u_{M} further, it can be seen from Figs. 8 and 9 that the estimated PZT microactuator's displacement y_{M}^* still resembles y_{M} measured from the LDV well with high SNR at nanometer resolution and accuracy even when the PZT microactuator is actuating at ± 5 and ± 10 nm in radial directions.

The measured y_{M} from the LDV becomes distorted when the PZT microactuator is actuating at about ± 5 nm in radial directions, as shown in Fig. 9. However, the PZT SNR is low only when the PZT microactuator is actuated to less than 2 nm (not shown), which makes the displacement estimation circuit H_{B} comparable to the measurements from the LDV in nanometer resolution.

2) Correlation Analysis: By setting the peak-to-peak level of u_{M} to 2 V corresponding to the PZT microactuator actuating at about ± 8 nm in radial directions, the frequency response of the measured PZT microactuator's displacement from LDV y_{M} to the estimated PZT microactuator's displacement y_{M}^* is shown in Fig. 10.

It can be seen from Fig. 10 that the estimated PZT microactuator's displacement y_{M}^* correlates well with measured PZT microactuator's displacement from LDV y_{M} from about 300 Hz onward even at small displacements of ± 8 nm. This makes the displacement estimation circuit H_{B} effective only in the higher

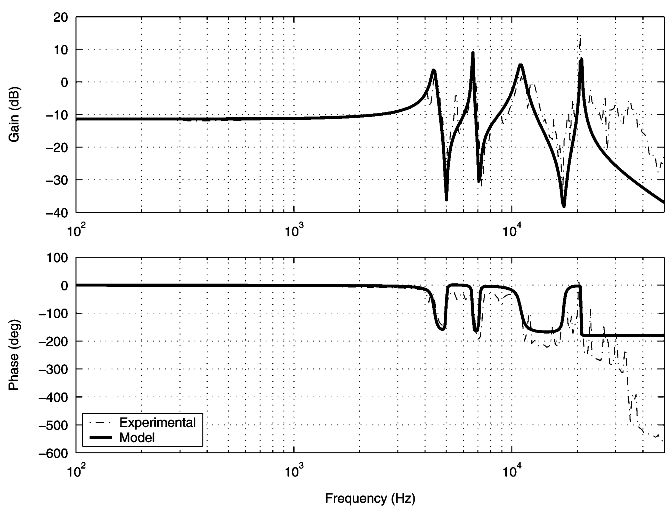

Fig. 11. Frequency response of PZT microactuator.

frequencies, which is tolerable as low frequency error rejection is mainly done by the VCM. The high frequency accuracy is also essential for effective inner-loop compensation AMD control to actively damp the high-frequency PZT microactuator's torsion and sway modes to be discussed in future sections.

IV. SSA–DMS Dual-Stage Controller Design

With the measured PES and online estimated PZT microactuator's displacement y_{M}^{*}, we can proceed to design the SSA–DMS dual-stage track-following and AMD controllers in Fig. 2. The designs of the VCM controller C_{V} and the PZT microactuator controller C_{M} are discussed in Sections IV-A and IV-C, respectively. The AMD controller design using y_{M}^{*} is discussed in Sections IV-B.

A. VCM Controller

Suppose the dominant VCM resonant modes are compensated for by notch filters and the compensated model can be approximated by a double integrator in the frequencies of interest. A lag-lead compensator recommended in [4] is used as the VCM controller. This design methodology uses the lag portion of the controller to increase the low-frequency gain for low-frequency disturbance rejection and tracking accuracy. The lead portion of the controller increases the phase margin to ensure stability during crossover region. This design also requires the servo designer to tune only one parameter α for the desired gain crossover frequency f_{V}. A slight modification is made and the controller takes the following form [12]:

$$C_{\mathrm{V}}(s) = K_{\mathrm{V}} \frac{s + \frac{2\pi f_{\mathrm{V}}}{2\alpha}}{s + 2\pi 10} \frac{s + \frac{2\pi f_{\mathrm{V}}}{\alpha}}{s + 2\alpha 2\pi f_{\mathrm{V}}} \tag{7}$$

with $5 < \alpha < 10$ used typically. K_{V} can be calculated by setting $|C_{\mathrm{V}}(j2\pi f_{\mathrm{V}})G_{\mathrm{V}}(j2\pi f_{\mathrm{V}})| = 1$.

B. AMD Controller

In conventional HDDs, noncollocation of actuators (VCM) and sensor (R/W head) exists. However with SSA, the collocation of PZT microactuator and PZT microactuator's displacement sensor issue is nearly achieved. The estimated PZT microactuator's displacement y_{M}^{*} can be used for many control methodologies, e.g., dual-input single-output (DISO) robust control synthesis. In this section, we present a robust AMD controller design for damping the PZT microactuator suspension's torsion modes and sway modes.

The PZT microactuator behaves like a pure gain in low frequencies coupled with a number of resonant poles and antiresonant zeros at high frequencies, as can be seen in Fig. 11.

The identified model $G_{\mathrm{M}}(s)$ is

$$\begin{aligned} G_{\mathrm{M}}(s) &\\ = 0.9875 \cdots &\\ \times \frac{s^2 + 2(0.01)(2\pi 5 \times 10^3)s + (2\pi 5 \times 10^3)^2}{s^2 + 2(0.05)(2\pi 4.41 \times 10^3)s + (2\pi 4.41 \times 10^3)^2} &\\ \times \frac{s^2 + 2(0.01)(2\pi 7.1 \times 10^3)s + (2\pi 7.1 \times 10^3)^2}{s^2 + 2(0.01)(2\pi 6.62 \times 10^3)s + (2\pi 6.62 \times 10^3)^2} &\\ \times \frac{s^2 + 2(0.03)(2\pi 17.3 \times 10^3)s + (2\pi 17.3 \times 10^3)^2}{s^2 + 2(0.07)(2\pi 11 \times 10^3)s + (2\pi 11 \times 10^3)^2} &\\ \times \frac{(2\pi 20.8 \times 10^3)^2}{s^2 + 2(0.001)(2\pi 20.8 \times 10^3)s + (2\pi 20.8 \times 10^3)^2}. & \end{aligned} \tag{8}$$

The PZT microactuator suspension has identified torsion modes at 4.31 and 6.52 kHz and sway mode at 21.08 kHz.

We propose an AMD controller $C_{\mathrm{D},i}(s)$ for each resonant mode i as

$$C_{\mathrm{D},i}(s) = K_{\mathrm{D},i} \frac{s + \frac{\omega_{n,i}}{\varepsilon_{\mathrm{i}}}}{s + \frac{\kappa_{\mathrm{i}}\omega_{n,i}}{\varepsilon_{\mathrm{i}}}} \frac{s + \omega_{n,i}}{s + \frac{\varepsilon_{\mathrm{i}}\omega_{n,i}}{\kappa_{\mathrm{i}}}} \tag{9}$$

to increase the damping ratios (hence smaller amplitudes) of the PZT microactuator suspension's torsion modes and sway mode. $K_{\mathrm{D},i}$ is set to ε_{i} in most cases. ε_{i} and κ_{i} are tuning parameters. $1 < \varepsilon_{\mathrm{i}} \leq P$ is chosen usually for robustness against natural frequency variations $P\%$, where $P < 3$ for most physical systems. $5 < \kappa_{\mathrm{i}} < 15$ is then chosen to determine the amount of phase lift required to stabilize the resonance mode at the natural frequency $\omega_{n,i}$. The overall AMD controller C_{D} is given by

$$C_{\mathrm{D}}(s) = \prod_{i=1}^{N} C_{\mathrm{D},i}(s) \tag{10}$$

where $N = 3$ in this case. Phase lead compensators are sometimes added to reduce the phase loss introduced by the AMD controllers and to increase the gain of the PZT microactuator's displacement for high-frequency mode detection. C_{D} can be thought of as a general case of traditional PPF vibration controller [3] with additional minimum phase zeros. The zeros prevent causality issues in PPF arrangements and improve the robust stability margin of the closed-loop system, as will be illustrated later. The proposed AMD controller in essence increases

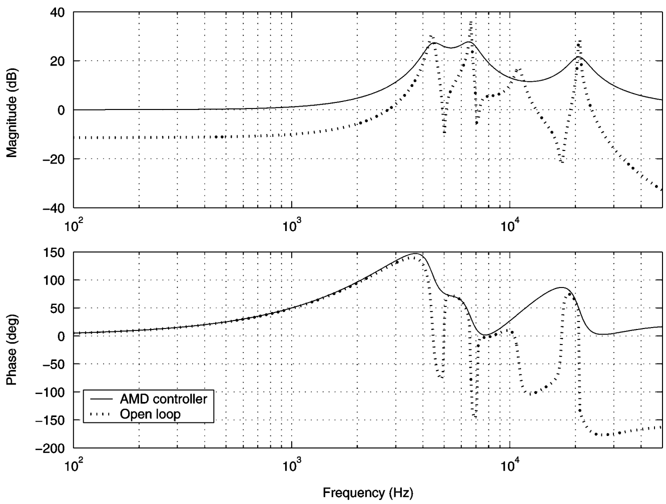

Fig. 12. Simulated frequency responses of PZT microactuator with AMD.

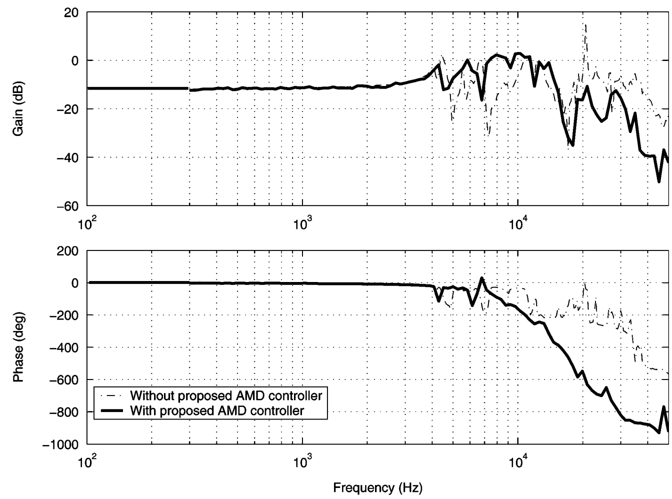

Fig. 13. Experimental frequency responses of PZT microactuator.

the gain of each resonant mode but stabilizes the PZT microactuator loop using a phase lead from the zeros at $(\omega_{n,i}/\varepsilon_{\mathrm{i}})$, which is a common result when using optimal control methods such as H_∞ loop shaping techniques.

Assuming that the PZT micro-actuator G_{M} has resonant modes at natural frequencies $\omega_{n,i}$ with the AMD controller C_{D} in the feedback path as shown in Fig. 2. The following equation closed-loop equation holds:

$$\frac{y_{\mathrm{M}}(s)}{u_{\mathrm{M}}(s)} = \frac{G_{\mathrm{M}}(s)}{1 + C_{\mathrm{D}}(s)G_{\mathrm{M}}(s)} \tag{11}$$

if the closed-loop system is stable. The gains of the modes are suppressed by the AMD controller at the frequencies $\omega_{n,i}$ of the resonant modes effectively by a factor of $(1/|C_{\mathrm{D}}(j\omega_{n,i})|)$

$$\begin{aligned}\left|\frac{y_{\mathrm{M}}(j\omega_{n,i})}{u_{\mathrm{M}}(j\omega_{n,i})}\right| &= \left|\frac{G_{\mathrm{M}}(j\omega_{n,i})}{1 + C_{\mathrm{D}}(j\omega_{n,i})G_{\mathrm{M}}(j\omega_{n,i})}\right| \\ &\approx \frac{|G_{\mathrm{M}}(j\omega_{n,i})|}{|C_{\mathrm{D}}(j\omega_{n,i})G_{\mathrm{M}}(j\omega_{n,i})|} \\ &= \frac{1}{|C_{\mathrm{D}}(j\omega_{n,i})|}\end{aligned} \tag{12}$$

if $|C_{\mathrm{D}}(j\omega_{n,i})G_{\mathrm{M}}(j\omega_{n,i})| \gg 1$.

The simulated frequency responses of AMD controller $C_{\mathrm{D}}(s)$ and the open-loop transfer function $C_{\mathrm{D}}(s)G_{\mathrm{M}}(s)$ are shown in Fig. 12. With $C_{\mathrm{D}}(s)$ in the feedback path as shown in Fig. 2 and (11), the loop is closed to damp the PZT microactuator suspension's torsion modes and sway mode. Fig. 13 shows that the PZT microactuator suspension's torsion modes at 4.31 and 6.52 kHz as well as sway mode at 21.08 kHz are all damped by the AMD controller C_{D}. The oscillations causing deviation of the R/W head from the track center during reading process are hence greatly reduced.

However, from Fig. 13, it can also be seen that the proposed AMD controller $C_{\mathrm{D}}(s)$ is more effective in suppressing the sway mode of the PZT microactuator at 21.08 kHz (>30 dB) than the torsion modes at 4.31 and 6.52 kHz ($\approx$5 dB). This is apparent as the estimated PZT microactuator's displacement y^*_{M} from the displacement estimation circuit H_{B} is only effective in measuring in-plane components (making in-plane sway modes controllable) of the PZT microactuator and not the torsion modes (out-of-plane weakly controllable modes). The PZT microactuator's displacement estimation circuit H_{B} is a scalar signal and hence the control effectiveness of the system is reduced due to more degrees-of-freedoms (DOFs) in the PZT microactuator's suspension than control inputs.

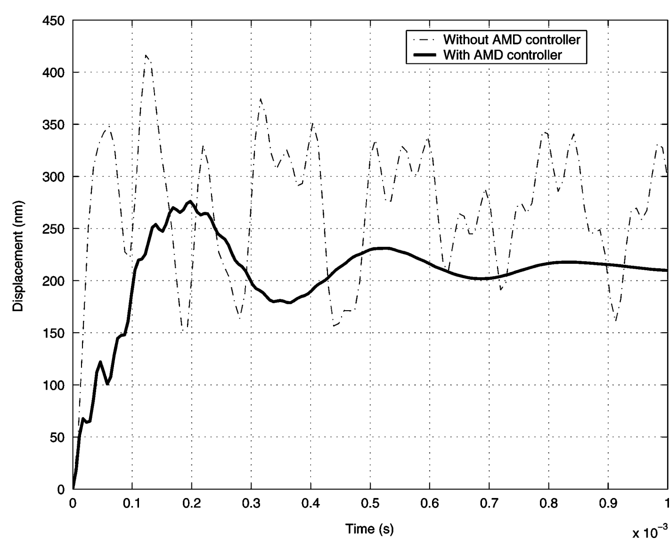

Fig. 14. Simulated step responses of PZT microactuator with and without AMD.

The simulated step responses of the PZT microactuator with and without the proposed AMD controller C_{D} are shown in Fig. 14. The transfer function of the step response with AMD

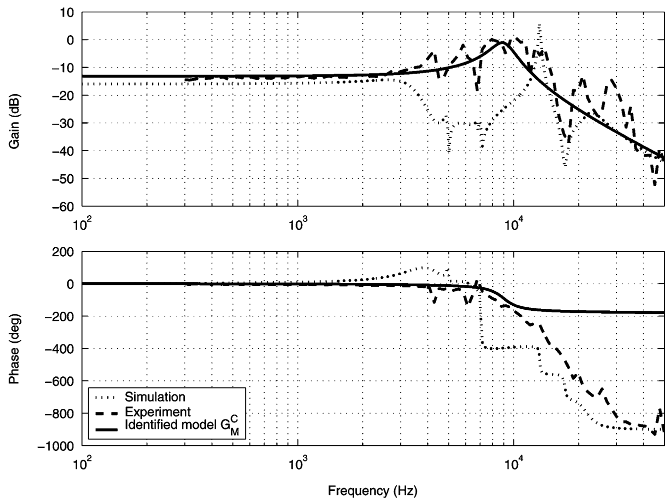

Fig. 15. Identified model of PZT microactuator with AMD control.

controller $y_{\mathrm{AMD}}(s)$ is given by

$$\begin{aligned} y_{\mathrm{AMD}}(s) &= \frac{1260897508.4794}{s(s^2+7380s+3.808e8)}\cdots \\ &\times \frac{(s+3.142e5)^2(s^2+5542s+7.678e8)}{(s^2+1148s+9.809e8)(s^2+2.51e4s+1.468e9)} \\ &\times \frac{(s^2+314.2s+9.87e8)(s^2+8319s+1.73e9)}{(s^2+539.3s+1.958e9)(s^2+4.074e4s+6.199e9)} \\ &\times \frac{(s^2+446.1s+1.99e9)(s^2+3261s+1.182e10)}{(s^2+5.717e5s+8.846e10)(s^2+1.208e4s+1.232e10)} \\ &\times \frac{s^2+2.614e4s+1.708e10}{s^2+1.644e4s+4.248e10}. \end{aligned} \tag{13}$$

C. PZT Microactuator Controller

With the main resonant modes of the PZT microactuator dampened, we proceed to identify the mathematical model of the PZT microactuator with AMD control. In this section, a track-following controller $C_{\mathrm{M}}(s)$ is designed for this identified model.

Let the transfer function of the PZT microactuator with AMD control from $u_{\mathrm{M}}(s)$ to $y_{\mathrm{M}}(s)$ be $G_{\mathrm{M}}^{\mathrm{C}}(s)$ where the superscript C indicates the presence of AMD controller. Using a second-order model, we identify $G_{\mathrm{M}}^{\mathrm{C}}$ as

$$\begin{aligned} G_{\mathrm{M}}^{\mathrm{C}}(s) &= 0.25\frac{(2\pi 9\times 10^3)^2}{s^2+2(0.04)(2\pi 9\times 10^3)s+(2\pi 9\times 10^3)^2}. \end{aligned} \tag{14}$$

The frequency responses from the experiment and mathematical model are plotted in Fig. 15. A low-order model is used for identifying $G_{\mathrm{M}}^{\mathrm{C}}$, which suffices as the gain stabilization of the PZT microactuator loop is used and the amplitudes of the PZT microactuator's resonant modes with AMD control are all very small.

Using the model of $G_{\mathrm{M}}^{\mathrm{C}}$, the PZT microactuator track-following controller of the form

$$C_{\mathrm{M}}(s) = K_{\mathrm{M}}\frac{1}{s^2}\frac{s+2\pi\frac{f_{\mathrm{M}}}{\beta}}{s+2\pi\beta f_{\mathrm{M}}} \tag{15}$$

is used to control $G_{\mathrm{M}}^{\mathrm{C}}$. Where f_{M} is the gain crossover frequency of the open loop PZT microactuator path and β is a tuning parameter for intended disturbance attenuation. $1 < \beta \leq 1.2$ is used typically, and K_{M} can be found with the relation $|C_{\mathrm{M}}(j2\pi f_{\mathrm{M}})G_{\mathrm{M}}(j2\pi f_{\mathrm{M}})| = 1$.

The PZT microactuator controller C_{M} is in essence a double integrator in series with a lead compensator. The lead compensator is added to improve phase margin at the gain crossover frequency and hence closed-loop stability in the PZT microactuator loop. Integrators are placed to ensure steady-state accuracy in the PZT microactuator loop required for fast tracking and error rejection. Also, the integrators are essential to test the effectiveness of the bridge circuit in estimating the PZT microactuator's displacement and at the same time filter the high-frequency noise in the displacement estimation circuit. β can be used to tune the damping ratio of the closed-loop system. For implementation purposes, a slight modification to the above proposed controller in (15) becomes

$$C_{\mathrm{M}}(s) = K_{\mathrm{M}}\frac{\sigma^2}{(s+\sigma)^2}\frac{s+2\pi\frac{f_{\mathrm{M}}}{\beta}}{s+2\pi\beta f_{\mathrm{M}}} \tag{16}$$

where σ is chosen to be $\sigma < 100$. This practical modification prevents a large low-frequency gain, which saturates the PZT microactuator and causes integrator windup.

V. System Evaluation

In this section, we investigate the robustness of the proposed AMD controller $C_{\mathrm{D}}(s)$. The performance of the proposed dual-stage control topology, sensitivity transfer functions of the VCM loop, PZT microactuator loop, and dual-stage loop are presented. The 3σ PES of using the different control schemes are also compared.

A. Robustness Analysis

To illustrate the robustness of the proposed AMD controller C_{D}, we carry out simulations with $\pm 10\%$ shift in natural frequencies of the modes in the PZT microactuator, as shown in Fig. 16.

The corresponding closed-loop transfer functions and step responses are shown in with the same designed AMD controller $C_{\mathrm{D}}(s)$ as shown in Figs. 17 and 18, respectively. From these figures, it can be seen that the proposed AMD controller C_{D} is robust to resonant frequencies shifts up to $\pm 10\%$ using phase stabilization, hence avoiding the use of notch filters required for attenuating the gain of the modes. This method avoids the use of digital notch filters to attenuate the gain of the resonance modes as they are sensitive to transients of residual vibrations [15] and not robust to parametric variations. Shifts in

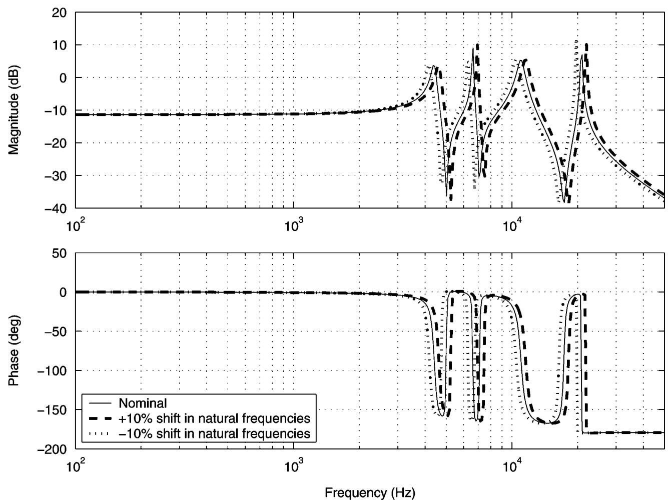

Fig. 16. Frequency responses of PZT microactuator with $\pm 10\%$ shift in natural frequencies.

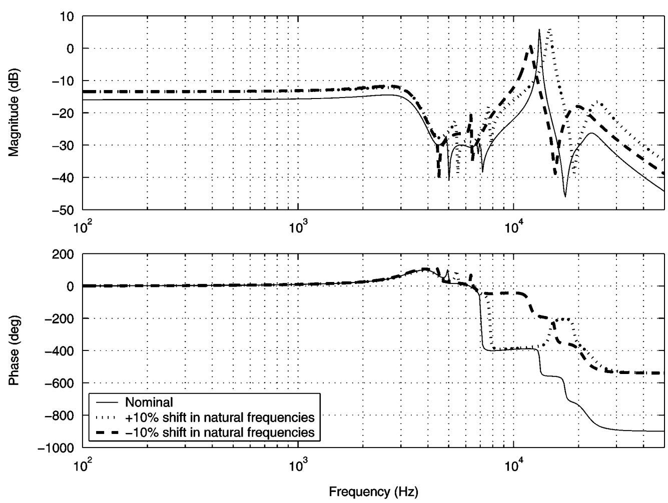

Fig. 17. PZT microactuator's inner closed-loop transfer functions.

natural frequencies often results in mode splitting and spill-over phenomenon, which compromises the closed-loop stability of the closed-loop system.

B. Decoupling Analysis

Referring to the SSA–DMS dual-stage control topology in Fig. 2, the following equations hold:

$$L_{\mathrm{D}} = (1 + C_{\mathrm{M}}G_{\mathrm{M}})C_{\mathrm{V}}G_{\mathrm{V}} + C_{\mathrm{M}}G_{\mathrm{M}} \tag{17}$$

$$\begin{aligned} S_{\mathrm{D}} &= \frac{1}{(1 + C_{\mathrm{M}}G_{\mathrm{M}})(1 + C_{\mathrm{V}}G_{\mathrm{V}})} \\ &= S_{\mathrm{M}}S_{\mathrm{V}} \end{aligned} \tag{18}$$

$$T_{\mathrm{D}} = \frac{(1 + C_{\mathrm{M}}G_{\mathrm{M}})C_{\mathrm{V}}G_{\mathrm{V}} + C_{\mathrm{M}}G_{\mathrm{M}}}{(1 + C_{\mathrm{M}}G_{\mathrm{M}})(1 + C_{\mathrm{V}}G_{\mathrm{V}})} \tag{19}$$

where $L_{\mathrm{D}}, S_{\mathrm{D}}$, and T_{D} are the dual-stage open loop, sensitivity, and complementary sensitivity transfer functions, respectively. S_{V} and S_{M} are the sensitivity transfer functions of the VCM path and PZT microactuator path, respectively.

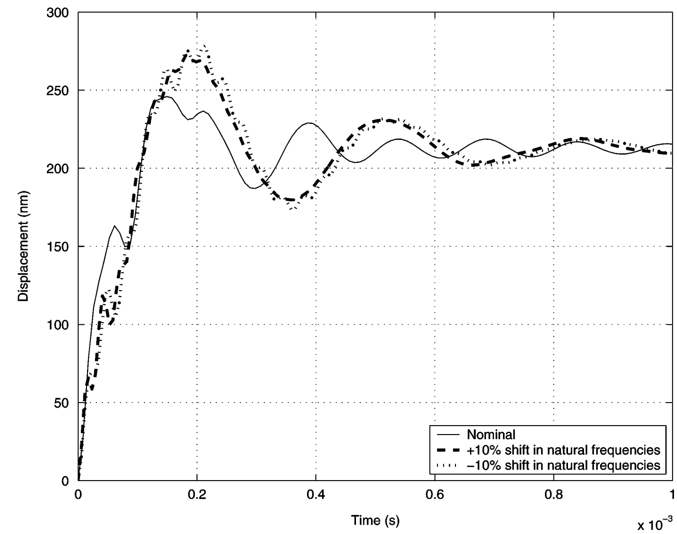

Fig. 18. Simulated step responses of PZT microactuator with $\pm 10\%$.

The sensitivity transfer function of the dual-stage servo system S_{D} is the product of the sensitivities of the VCM path and PZT microactuator path. As such, these sensitivity transfer functions are a measure of the extent of decoupling between the VCM path and PZT microactuator path.

For our design and experiment, we set f_{M} to be about 3 kHz. This high-gain crossover frequency—translating directly into a high dual-stage open-loop gain crossover frequency—is normally not achievable without AMD control, as the first dominant resonant mode of the PZT suspension-based microactuator is usually at 5–10 kHz. As no notch filters are used, two integrators are used for a high-gain reduction rate of about -40 dB/dec after gain crossover frequency f_{M} for closed-loop stability by keeping loop gain less than unity. The integrators are also important in sensitivity optimization via loop shaping of the dual-stage open-loop transfer function. The high roll-off rate after f_{M} causes the dual-stage open loop in the Nyquist plot to avoid the unit circle centered at $-1 + j0$, a region where feedback increases the sensitivity rather than decreasing it. The simulated sensitivity transfer functions of the VCM loop S_{V}, PZT loop S_{M}, and dual-stage loop with and without AMD are shown in Fig. 19.

The experimental sensitivity transfer functions $S_{\mathrm{V}}, S_{\mathrm{M}}$, and S_{D} are shown in Fig. 20. It can be seen from the sensitivity transfer functions that indeed $S_{\mathrm{D}} = S_{\mathrm{V}}S_{\mathrm{M}}$. However, because of the high gain feedback from the SSA loop, the low-frequency gain of the PZT microactuator in C_{M} is decreased to prevent saturation of the PZT microactuator. The estimated PZT microactuator's displacement y_{M}^{*} decouples the VCM path and PZT microactuator path into two distinct loops for individual path's sensitivity optimization. This method of using the real-time PZT microactuator's displacement estimation y_{M}^{*} is far more accurate and robust to parameter as well as environmental variations. S_{D} is shaped independently such that the lag portion of the VCM controller C_{V} is used for low-frequency disturbance rejection capabilities and tracking performance while the AMD

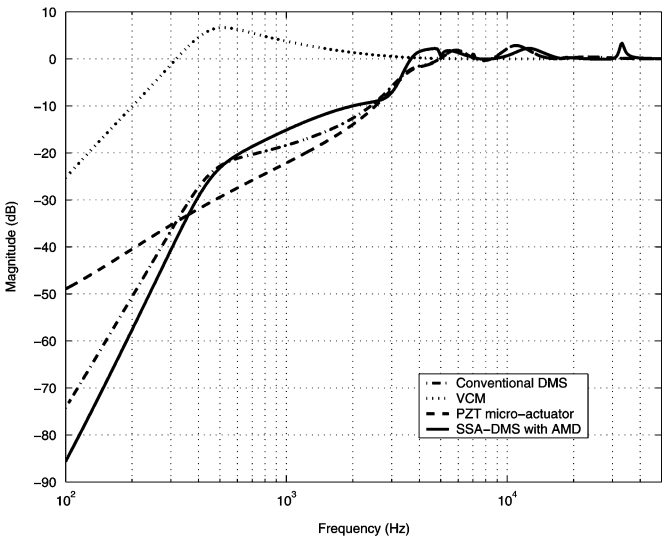

Fig. 19. Simulated sensitivity transfer functions of different control schemes.

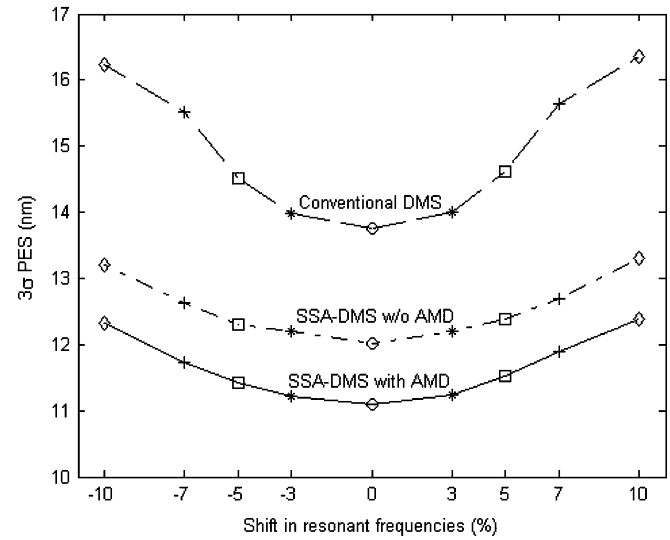

Fig. 21. Comparison of 3σ PES with different control schemes.

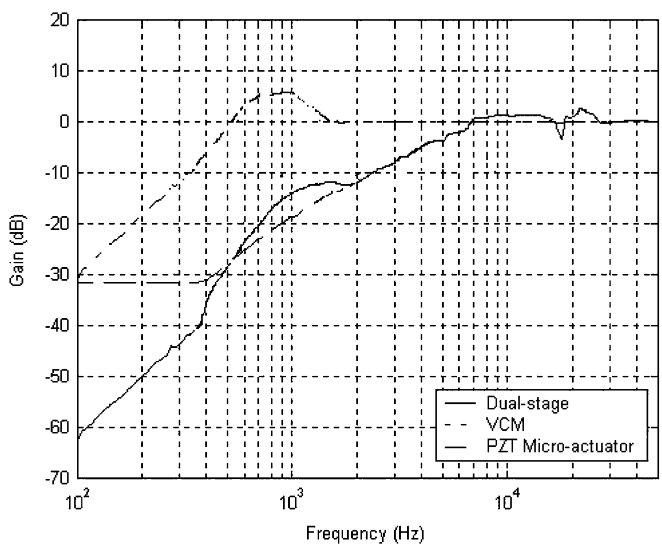

Fig. 20. Experimental sensitivity transfer functions using proposed SSA–DMS dual-stage control topology.

controller C_{D} and integrators in the PZT microactuator controller C_{M} are used to ensure a low hump in the high-frequency sensitivity after crossover frequency. The low-sensitivity hump retains good disturbance rejection capabilities and avoids amplification of output disturbances at higher frequencies [12].

C. 3σ PES

For simulation purposes, additive zero mean white noise with variance of 0.01 is added to the PZT microactuator's displacement to mimic sensing noise in the PZT elements. The 3σ PES of different control schemes used in the PZT microactuator loop for a dual-stage HDD is shown in Fig. 21, using vibration and noise models in [2].

The conventional DMS scheme uses digital notch filters to attenuate the gain of the resonant modes in the PZT microactuator, as depicted in Fig. 1. In the SSA–DMS scheme, digital notch filters together with $C_{\mathrm{D}} = 0$ are used, as shown in Fig. 2. The main difference between the conventional- and SSA–DMS schemes is that SSA–DMS is able to pick up real-time PZT microactuator's displacement while the conventional DMS scheme relies on an off-line estimator to estimate the displacement. The SSA–DMS with AMD control topology includes the proposed AMD controller C_{D} to damp the PZT microactuator's torsion modes and sway modes.

It can be seen that AMD control is robust for $\pm 10\%$ shifts in frequencies of the resonant modes ω_{R}. When SSA–DMS and AMD are employed simultaneously, better servo positioning capabilities are achieved with a reduction of up to 20% in 3σ PES.

VI. Conclusion

In this paper, we use SSA to construct a cheap and collocated PZT microactuator's displacement sensor with nanoposition resolution. The proposed displacement estimation circuit H_{B} estimates the PZT microactuator's displacement y_{M} with high correlation and high SNR without compromising the effective actuation of the PZT microactuator. y_{M}^{*} is used to design a robust AMD controller to actively damp the PZT microactuator suspension's torsion modes and sway mode, as well as decouple the dual-stage loop. Experimental results show the proposed dual-stage servo loop is effectively decoupled, and sensitivities in the VCM path and PZT microactuator path can be optimized individually to obtain a low-sensitivity hump servo system. An improvement of 3σ PES by up to 20% is also observed when both SSA and AMD control are employed simultaneously. Future works include applying to servo track writing (STW) technologies as well as servo test stands for higher kilo tracks per inch demonstrations.

ACKNOWLEDGMENT

The authors are thankful to Prof. S.-F. Ling for his advice during a discussion held at the Centre of Mechanics of Micro-Systems, Nanyang Technological University, Singapore.

REFERENCES

[1] B. M. Chen, T. H. Lee, and V. Venkataramanan, *Hard Disk Drive Servo Systems*, Advances in Industrial Control Series. Berlin, Germany, London: Springer-Verlag, 2002.
[2] C. Du, J. Zhang, and G. Guo, "Vibration analysis and control design comparison of fluid bearing and ball bearing HDDs," in *Proc. Amer. Cont. Conf.*, 2002, pp. 1380–1385.
[3] M. I. Friswell and D. J. Inman, "The relationship between positive position feedback and output feedback controllers," *Smart Mater. Struct.*, vol. 8, pp. 285–291, 1999.
[4] G. Guo, D. Wu, and T. C. Chong, "Modified dual-stage controller for dealing with secondary-stage actuator saturation," *IEEE Trans. Magn.*, vol. 39, no. 6, pp. 3587–3592, Nov. 2003.
[5] F. Y. Huang, W. Imaino, F. Lee, and T. Semba, "Active damping in HDD actuator," *IEEE Trans. Magn.*, vol. 37, no. 2, pp. 847–849, Mar. 2001.
[6] M. Karaman and W. C. Messner, "Robust dual-stage HDD track follow control systems design for hand off shaping," in *Asia-Pacific Magn. Record. Conf. Dig.*, 2002, pp. BA5-01–BA5-02.
[7] S.-H. Lee, C. C. Chung, and C. W. Lee, "High frequency vibration rejection in hard disk drives," in *Proc. IIP/ISPS Joint MIPE*, 2003, pp. 24–25.
[8] Y. Li, R. Horowitz, and R. Evans, "Vibration control of a PZT actuated suspension dual-stage servo system using a PZT sensor," *IEEE Trans. Magn.*, vol. 39, no. 2, pp. 932–937, Mar. 2003.
[9] S.-F. Ling and Y. Xie, "Monitoring structural integrity using a piezoceramic inertial actuator cum sensor," *J. Sound Vib.*, vol. 247, no. 4, pp. 731–737, 2001.
[10] S. O. R. Moheimani, "A survey of recent innovations in vibration damping and control using shunted piezoelectric transducers," *IEEE Trans. Contr. Syst. Technol.*, vol. 11, no. 4, pp. 482–494, Jul. 2003.
[11] C. K. Pang, G. Guo, B. M. Chen, and T. H. Lee, "Nanoposition sensing and control in HDD dual-stage servo systems," in *IEEE Int. CCA*, 2004, pp. 551–556.
[12] C. K. Pang, D. Wu, G. Guo, T. C. Chong, and Y. Wang, "Suppressing sensitivity hump in HDD dual-stage servo systems," *Microsyst. Technol.*, vol. 11, no. 8–10, pp. 653–662, Aug. 2005.
[13] K. Peng, B. M. Chen, T. H. Lee, and V. Venkataramanan, "Design and implementation of a dual-stage actuated HDD servo system via composite nonlinear control approach," *Mechatronics*, vol. 14, pp. 965–988, 2004.
[14] T. Semba, T. Hirano, J. Hong, and L-S. Fan, "Dual-stage servo controller for HDD using MEMS microactuator," *IEEE Trans. Magn.*, vol. 35, no. 5, pp. 2271–2273, Sep. 1999.
[15] H. Uchida and T. Semba, "A study of the residual vibration during the seek-settling period for hard disk drives," in *Asia-Pacific Magn. Record. Conf. Dig.*, 2000, pp. MP19-1–MP19-2.
[16] R. W. Wood, J. Miles, and T. Olson, "Recording technologies for terabit per square inch systems," *IEEE Trans. Magn.*, vol. 38, no. 4, pp. 1711–1718, Jul. 2002.
[17] H. Yamada, M. Sasaki, and Y. Nam, "Control of a microactuator for hard-disk drives using self-sensing," presented at the 8th IEEE Int. Workshop on Advanced Motion Control, Mar. 2004.

Chee Khiang Pang (S'04) was born in Singapore in 1976. He received the B.Eng. (honors) and M.Eng. degrees from the National University of Singapore (NUS), Singapore, in 2001 and 2003, respectively, both in electrical and computer engineering. He is currently pursuing the Ph.D. degree in electrical and computer engineering from National University of Singapore.

From February to June 2003, he was a Visiting Scholar in the School of Information Technology and Electrical Engineering, University of Queensland, Brisbane, QLD, Australia. His current research interests include dynamic systems and control, multisensing and servo control in dual-stage HDDs, and probe-based storage systems.

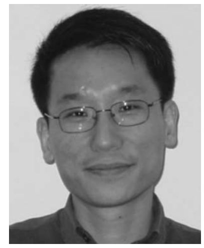

Guoxiao Guo (S'95–M'96–SM'05) received the B.Eng. and M.Eng. degrees from Tsinghua University, Beijing, China, and the Ph.D. degree from the School of Electrical and Electronic Engineering, Nanyang Technological University (NTU) Singapore, in 1989, 1994, and 1997, respectively, all in electrical engineering.

In 1995, he joined the A*STAR Data Storage Institute, Singapore, as a Research Engineer and later was the Manager of the Mechatronics and Recording Channel Division. He is also an Adjunct Fellow at the National University of Singapore, Singapore, and Adjunct Associate Professor at the NTU. He has published over 50 refereed journal papers and holds 6 patents. His research focuses on vibration analysis, sensing and control, mechatronics and MEMs, and nonlinear and robust control for achieving nanopositioning systems in ultrahigh density magnetic recording.

Dr. Guo was the Publication Chairman/Co-chair for the Asia-Pacific Magnetic Recording Conferences 2000 (Tokyo, Japan), 2002 (Singapore), and 2004 (Seoul, Korea). He is currently serving as the Associate Editor of the IEEE TRANSACTIONS ON CONTROL SYSTEMS TECHNOLOGY.

Ben M. Chen (S'89–M'91–SM'00) was born in Fuqing, Fujian, China, in 1963. He received the B.S. degree in computer science and mathematics from Xiamen University, Xiamen, China, in 1983, the M.S. degree in electrical engineering from Gonzaga University, Spokane, WA, in 1988, and the Ph.D. degree in electrical and computer engineering from Washington State University, Pullman, in 1991.

From 1992 to 1993, he was an Assistant Professor in the Electrical Engineering Department, State University of New York, Stony Brook. In 1993, he joined the Department of Electrical and Computer Engineering, National University of Singapore, Singapore, where he is currently a Professor. He is the author/coauthor of seven research monographs including *Hard Disk Drive Servo Systems* (New York: Springer-Verlag, 1st ed. 2002 and 2nd ed. 2006); *Linear Systems Theory: A Structural Decomposition Approach* (Boston: Birkhäuser, 2004); *Robust and H_∞ Control* (New York: Springer-Verlag, 2000). His current research interests include robust control, systems theory, and control applications.

Dr. Chen has served as the Associate Editor of the IEEE TRANSACTIONS ON AUTOMATIC CONTROL and the *Asian Journal of Control* and is currently serving as the Associate Editor of *Automatica, Control* and *Intelligent Systems* and *Systems and Control Letters*.

Tong Heng Lee (M'90) received the B.A. degree (honors) in the engineering tripos from Cambridge University, Cambridge, U.K., in 1980 and the Ph.D. degree from Yale University, New Haven, CT, in 1987.

He is a Professor in the Department of Electrical and Computer Engineering, National University of Singapore, Singapore. He has coauthored three research monographs and holds four patents (two of which are in the technology area of adaptive systems and the other two are in the area of intelligent mechatronics). His research interests include the areas of adaptive systems, knowledge-based control, intelligent mechatronics, and computational intelligence.

Dr. Lee serves as an Associate Editor of the IEEE TRANSACTIONS IN SYSTEMS, MAN AND CYBERNETICS, *Automatica*, *Control Engineering Practice* (an IFAC journal), the *International Journal of Systems Science*, and the *Mechatronics Journal*. He was a recipient of the Cambridge University Charles Baker Prize in Engineering.